CFD Reproduction of Nonlinear Loads on a Vertical Column during Extreme Irregular Wave Events

Erin E. Bachynski, *
Associate Professor
Dept. of Marine Technology,Norwegian University of Science and Technology (NTNU)
Trondheim, Norway
Email: erin.bachynski@ntnu.no

Csaba Pákozdi
Research Scientist
SINTEF Ocean (former MARINTEK)
Trondheim, Norway
Email: csaba.pakozdi@sintef.no

Anders Östman
Senior Research Scientist
SINTEF Ocean (former MARINTEK)
Trondheim, Norway
Email: anders.ostman@sintef.no

Carl Trygve Stansberg
previously Norwegian Marine Technology Research Institute (MARINTEK)
Trondheim, Norway
Email: ctstansberg.marinteknikk@gmail.com

Recently, a method for numerical reproduction of measured irregular wave events has been developed. The measured motion of the wave maker flaps defines the wave kinematics at the boundary of the numerical simulation in order to generate the waves. When such data are not available, the control signal of the wave maker can, instead, be generated from a given free surface elevation following the same procedure as in model tests.

This procedure is applied to a model test case with extreme irregular wave events and resulting nonlinear global wave loads on a vertical cylinder, focusing on higher-order ringing excitation. The purpose of the investigation is twofold: 1) to validate the wave reconstruction procedure, and 2) to validate the resulting CFD ringing loads with the given waves. In order to better understand the frequency content in the CFD-generated loads, wavelet analysis as well as the response of a single degree-of-freedom (SDOF) oscillator are examined and compared with the corresponding results for the 3rd order wave forcing based on the MacCamy-Fuchs (MF) and Faltinsen, Newman, Vinje (FNV) formulations.

The results show generally good agreement between CFD and experiment both in the waves and in the loads; discrepancies found in the loads mainly originate from corresponding uncertainties in the wave reconstruction. Wave breaking may be one source of uncertainty. The MF+FNV formulation showed reasonable prediction of the maximum responses of an SDOF oscillator, but could not capture the loads well at all of the important frequencies.

1 Introduction

Irregular, steep waves can impart high-frequency hydrodynamic loads which result in ringing-type responses on flexible offshore structures such as tension leg platforms, gravity-based structures, and offshore wind turbines. Model tests and efficient numerical models have long been employed in order to study these load mechanisms and responses [1–4]. Computational fluid dynamics (CFD) methods are also becoming more applicable, and allow for bet-

*Address all correspondence to this author.

ter understanding of some of the nonlinear flow phenomena. Local effects around the cylinder, as well as the spatial distribution of the wave kinematics over time, are among the additional information that can be gathered through CFD simulations. Still, reproduction of specific events from irregular wave tests in the laboratory remains challenging and time-consuming.

For the CFD reproduction of measured irregular wave events observed in model tests, SINTEF Ocean typically uses the wave maker control signal as input to a numerical wave tank. Hence, the motion of the flaps defines the wave kinematics at the boundary of the numerical simulation in order to generate the waves. The same approach was successfully used by Perić et al [5].

When the measured wave flap motion is not available, or if the distance from the wave maker to the model in the numerical wave tank should be shortened in order to reduce the computational demands, the control signal of the wave maker can be generated from a given free surface elevation at a point in space through backward wave propagation to a virtual wave maker. Following this procedure automatically gives the possibility to subsequently reproduce the numerical wave experimentally using the obtained control signal. Iteration may be required in order to choose the desired control signal [6], which can be a time-consuming process when CFD codes are applied. Alternatively, one could use analytic wave theory to define the boundary condition for the numerical simulation [7]. In the described procedure, the latter choice is not followed, in order to maintain the link between the model test and the numerical simulation. Another alternative procedure, applied on a similar problem, has been presented in Kim et al. in 2012 ("Euler overlay method") [8] and [9]. In the present work, the control signal for a numerical wave maker is obtained based on linearly propagating the measured wave components back to a different (closer) location than the original wave maker. Rather than iteratively improving the wave maker control signal, the present work looks for the most similar wave signal at a different location - thus greatly reducing the computational cost.

The first topic of this paper is the validation of the procedure for reproducing measured time series of *wave elevations* for very steep random wave events. Model test data from SINTEF Ocean's 10 m deep towing tank extension, previously published by Stansberg in 1997 [10], are used for the irregular wave event validation.

The second topic of the paper is a validation of the resulting CFD loads against the measured *loads* on a vertical cylinder in deep water, and a comparison against a simplified numerical model (based on the MacCamy-Fuchs formulation of the first order wave loads and Johannessen's FNV formulation [1, 11, 12]). Based on the importance of the high-frequency loads for the response, an investigation of the high-frequency content of the loads is carried out through wavelet transformation and by studying the response of a single degree-of-freedom (SDOF) oscillator, thus extending the results presented in [13]. The CFD results have additionally been re-checked and updated in the present paper.

Two random wave events with large measured higher-order surge forces were chosen for study. Since one purpose of this work is to validate a general procedure where the numerical domain may need to be shorter than the experimental domain, the position of the wave maker in the numerical simulation was varied to check the accuracy. This yields different control signals than the ones used in the model test. The volume of fluid (VOF) model from the commercial solver Star-CCM+, considering inviscid flow, was used in the numerical simulation, since viscous forces are not anticipated to be of great importance for the ringing-type excitation in deep water [1]. Results from the free surface elevation at the position of the vertical cylinder (without the cylinder present) as well as the results from horizontal wave force measurements on the cylinder are examined.

Section 2 describes the procedure for generating the CFD control signal, while Section 3 describes the experimental data used for the validation. The CFD setup is detailed in Section 4, while the analytical hydrodynamic load model is presented in Section 5. The methods for comparing the high-frequency content of the loads are briefly described in Section 6 prior to the presentation of results and conclusions in Sections 7 and 8, respectively.

2 Generation of wave maker control signal

In the model tests, an FFT is used to generate an irregular wave realization. Any kind of energy spectrum may be specified, within the limitations given by physical laws of water waves at a given location. Complex Fourier amplitudes are then generated, each with its amplitude randomly chosen from a Rayleigh distribution around the "target" value for the chosen spectrum. Using the linear dispersion relationship between the wave number and the wave frequency, these complex Fourier amplitudes are then modified in order to account for the distance between the wave maker and the location. In order to reduce the effect of the "parasitic" waves, this distance is usually more than two times larger than the wavelength associated with a wave period equal to the peak period. The time series of the control signal is FFT generated from the multiplication of the modified complex Fourier amplitudes with the transfer function of the wave maker. The transfer function of the wave maker defines the relationship between the free surface elevation at the wave maker location and the motion of the wave maker's flaps.

If the target wave elevation includes steep and breaking waves, there are inherent errors in this procedure due to the limitations of the applied linear wave theory: the propagation of steep or breaking waves includes nonlinearities which are not modeled by linear theory. These limitations are usually rectified with an iterative process where the control signal is modified in order to get the correct wave elevation statistics at the correct location, as in [6, 7].

The same procedure is used in this study to generate the control signal for the numerical simulation, as illustrated in Fig. 1. The complex Fourier amplitudes are estimated from the inverse FFT of the measured time series at a distance of 38.6 m from the wave maker. The length of the time series is limited to 45 or 65 seconds in model scale. The complex

Fourier amplitudes are then modified in order to estimate the free surface elevation at 20 m distance from the location of the physical wave maker. The wave maker transfer function from the model test is used to generate the flap motion for the numerical wave maker (which is located 20 m downstream of the physical wave maker). This flap motion is the input for the CFD simulation. SINTEF Ocean's existing wave maker is implemented in the simulation (Fig. 2 and 4).

3 Brief review of experiments

Results from horizontal wave force measurements on vertical cylinders were presented by Stansberg [10]. The tests were carried out in SINTEF Ocean's 10 m deep towing tank extension, which measures 10 m x 80 m in the horizontal directions. The waves were generated in the direction along the longitudinal tank axis and the measurements were made at a distance 38.6 m from the wave maker. All data is given in model scale. The column was rigidly fixed to a stiff framework (Fig. 3). The integrated hydrodynamic force and pitching moment could be measured using the two force sensors, T1 and T2, to which the column was fixed.

The two wave events which were selected from the model tests are part of the same realization of an irregular sea state with significant wave height $H_s = 0.279$ m and peak period $T_p = 2.4$ s. The JONSWAP wave spectrum was applied with peak enhancement factor $\gamma = 1.7$.

4 CFD setup

4.1 Wave maker boundary conditions

In the present work, a numerical wave tank is used where the waves are generated by implementing a numerical wave maker in the simulation. The linear control signal results in a nonlinear wave by propagation through the numerical wave tank. Both implementations of wave makers in numerical simulation are used:

1. explicit
2. simplified.

The initial condition in the tank is still water in both cases.

In the explicit method, the motion of the two-flap wave generation mechanism is explicitly modelled in the CFD simulation (Fig. 4). Separate boundary patches are defined for each flap and these boundary patches are forced to move in a prescribed motion. The deformation of the computational mesh in the vicinity of the flap boundaries is modelled by means of a morphing mesh technique. The mesh motion using the morphing technique could become very time-consuming for the 3-D simulation with many cells [15]. The explicit method is only used for wave generation without the structure.

A simplified wave maker is used to reproduce irregular wave events with the structure in order to reduce the CPU time. In the simplified model, the wave generation is modelled on a stationary mesh and a transient velocity inlet condition is defined which simulates the wave-making device [14]. Both velocity and free surface elevation need to be prescribed at the boundary. The velocity at the flap boundary is calculated based on the kinematics of the wave maker. The unknown water level is calculated from the simulation with the explicit wave-maker model (without structure).

Both of the implementations are found to give the same wave elevation at the structure location.

A two-phased fluid VOF model is used to simulate water with free surface because Star-CCM+ does not offer one phase VOF model. The water is simulated as an inviscid and incompressible fluid and the air is simulated as an inviscid and incompressible gas. This physical model of the two phased inviscid fluid fluids has been successfully validated [5, 16].

4.2 Extents of the computational domain

The size of the CFD domain in the lateral and vertical directions is based on the dimension of the tank in the model tests. The size of the computational domain is therefore set to 10 m in the lateral direction, and half of the domain is simulated (applying symmetry). The water depth in the simulations is set to 10 m (as in the model tests). The top boundary was located 5 m above the undisturbed free surface. The length of the numerical domain is chosen based on the needed numerical beach (damping region). An overview of the extents of the numerical domain is presented in Table 1.

Table 1. Extents of the computational domain.

x [m]		y [m]		z [m]	
min.	max.	min	max	min	max
0	137	0	5	-10	5

4.3 Boundary conditions

The boundary conditions of the CFD simulations are presented in Fig 5. The different colors symbolize different boundary conditions:

1. red: the velocity inlet condition (inlet boundary at the location of the wave maker)
2. orange: the pressure outlet condition (top boundary)
3. grey: the wall condition with slip condition due to the inviscid fluid model (cylinder and side walls).
4. blue: symmetry condition.

4.4 Mesh topology

The volume mesh is shown in Figs. 6-7. The same mesh sizes and topology are used here as in [15] because we model the same wave tank with the same water depth and similar wave events. The total number of cells was approximately 6.1 million. The convergence studies and validation are presented in [15]. When simulating extreme steep or breaking

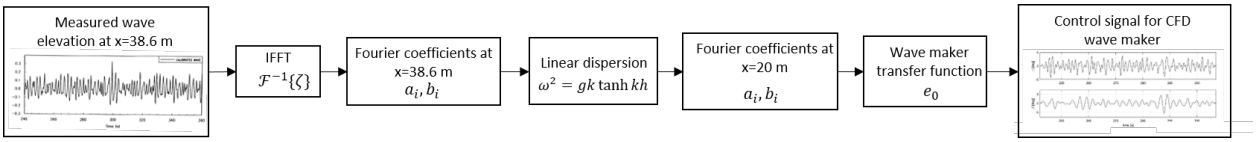

Fig. 1. Procedure for generating the wave maker control signal for CFD reproduction of an irregular wave event.

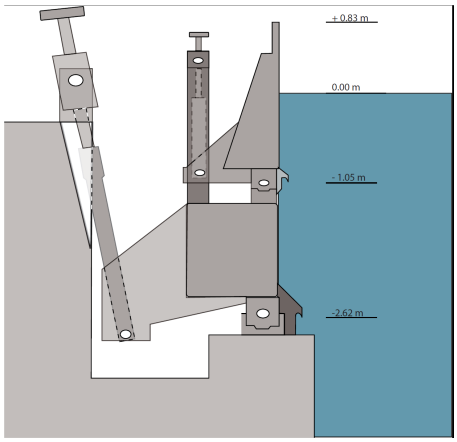

Fig. 2. SINTEF Ocean's BM1 wave maker [14].

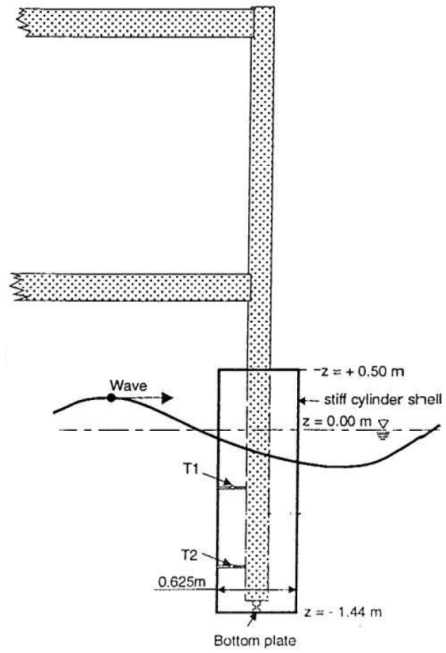

Fig. 3. Model setup [10]

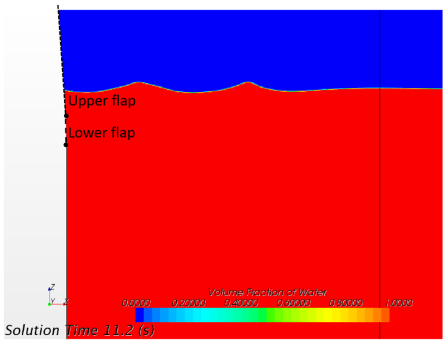

Fig. 4. Wave flaps in the simulation with explicit wave maker.

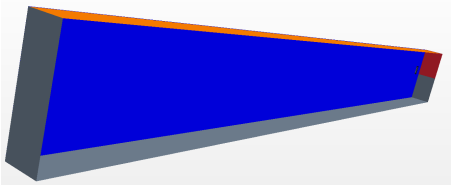

Fig. 5. Applied boundary conditions. All boundaries are visualized in the figure, except the side wall boundary at $y = 0$ m.

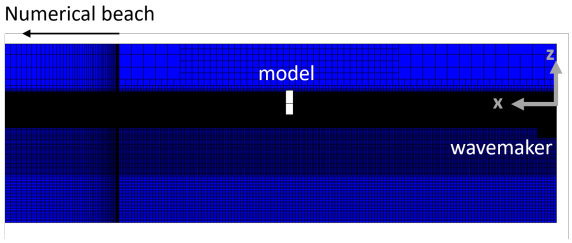

Fig. 6. The main part of the computation domain and the start of the stretched mesh part.

wave events, convergence studies are complicated by the fact that wave breaking may be missed by a coarse grid or predicted differently by several fine grids [17, 18] - and such events are not necessarily perfectly repeatable in a physical wave basin.

In order to reduce wave reflections, the STAR-CCM+ standard wave damping zone with a stretched mesh far behind the cylinder is used to dampen the waves (Fig. 6). The numerical domain is therefore longer than the physical tank.

5 Analytical hydrodynamic model

Simpler (analytical) formulations for the hydrodynamic loads are also included for comparison in the present work. The wavelength-to-diameter ratio based on the peak period of 2.4 s and diameter 0.625 m is 14.3. Although the cylinder can be considered slender for the most important waves in the irregular sea condition, the MacCamy-Fuchs solution of the potential flow problem was applied such that near-field diffraction effects would be included for shorter waves [11].

The long-wave assumption was nonetheless applied in the computation of second and third order wave loads. The FNV solution [1] was judged to be appropriate for the considered cylinder in deep water, and corresponds to the modeling which was applied in the original publication of these

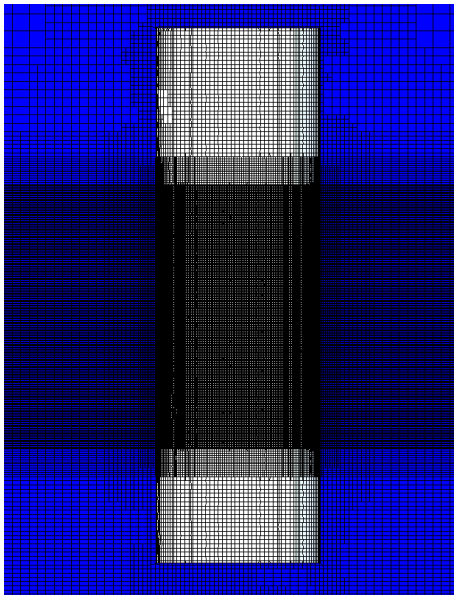

Fig. 7. Mesh in a longitudinal cut located at the centre of the geometry

experimental results [10]. Unlike the aforementioned paper, a bandwidth-limited sum-frequency formulation [12] for the second and third order force in irregular waves was applied in the present work. As discussed in [2], this newer formulation addresses some of the difficulties associated with a direct implementation of Newman's extension of the FNV formulation to irregular waves [19]: terms that do not decay at high frequency, as well as undesired difference-frequency terms. Johannessen's formulation includes only sum-frequency terms, and the bandwidth limitation removes interaction between components with significantly different frequency that may otherwise cause numerical problems.

It should be noted that the second order FNV formulation is applied here, despite some evidence that the full second-order sum-frequency quadratic transfer function may reduce the overprediction of the forces [20,21]. Furthermore, viscous drag effects are neglected in the simplified model, which is consistent with the CFD modeling.

6 Analysis of frequency content

Two approaches are applied in this paper for comparison of the frequency content of the obtained hydrodynamic loads: wavelet transformation, and the dynamic response of a single degree-of-freedom (SDOF) oscillator.

Continous wavelet transformations can be used to visualize the frequency content of the loads over time. In the present work, we apply a Morlet wavelet [22]. The CFD force signal is resampled at the same frequency as the experimental signal in the wavelet comparisons.

The SDOF oscillator in the dynamic response study is an inertia-spring-dashpot system, which is subjected to a moment defined by the horizontal force F_x multiplied by a constant arm h as excitation. The computed response x is a pitching rotation.

$$m\ddot{x} + c\dot{x} + kx = F_x h \tag{1}$$

In Eq. 1, c and k are chosen to give specific values of natural period (t_n) and critical damping ratio (ζ) while m represents an approximation of the moment of inertia of the scale model:

$$t_n = \frac{2\pi}{\sqrt{k/m}} \tag{2}$$

$$\zeta = \frac{b}{2\sqrt{mk}}. \tag{3}$$

The range of t_n is selected to be from 0.3 s to 0.9 s in model scale. Assuming a scale ratio between 1:40 ($D = 25$ m, as in the column of Snorre A [23]) and 1:30 ($D = 18.75$, similar to the column of Hutton [24] or Morpeth [25]), these t_n are representative of realistic TLP natural periods in pitch, 2-4.5 s in full scale. The obtained responses (x) are scaled by the static response (x_{ref}, Eq. 4) of the oscillator to the maximum measured hydrodynamic load (Eq. 4), such that the magnitude of the response can more easily be examined for all of the different SDOFs.

$$x_{ref} = \frac{\max\left(F_{meas}\right)}{k} \tag{4}$$

Typical values of TLP damping have been estimated to be roughly 1-2 % [26]. Although previous studies show that ringing responses are fairly insensitive to the damping level [27], three damping values (1 %, 2 %, and 5 % of critical damping) were applied in the simulations in order to account for variations.

The SDOF response was solved over the same time period regardless of the source of the load time series. For event A, 19 seconds prior to the event were used, while 22 seconds were used for event B. The initial condition of the oscillator was specified as $x = 0$, $\dot{x} = 0$, and the forcing function started with 4 seconds of ramp (half-sine multiplied with the forcing function).

7 Results

Two model test events (identified as event A and event B) with the measured largest higher-order surge force were chosen for the validation, and all results are shown in model scale. Event A corresponds to the largest horizontal force amplitude measured during the realization described in Section 3, while event B corresponds to the largest high-pass filtered horizontal force. The results for the wave calibration and hydrodynamic loading are presented in Section 7.1 for event A, and in Section 7.2 for event B.

7.1 Event A

7.1.1 Wave calibration

The results of the wave-only CFD simulation (wave calibration) are shown in Figs. 8-10. First, a comparison of the numerically estimated time series at different locations against the measured time series is presented in Fig. 8. The best match for the wave event was about 2.5 m downstream from the target location; the wave elevation at the "best match" location is seen in the top subplot of Fig. 10. Table 2 quantifies the differences between the measured and simulated wave elevation in terms of:

1. Crest height: the maximum wave elevation η_{max}
2. Rise time: the time between the zero-upcrossing at the time of maximum wave elevation
3. Steepness: the time derivative of the wave elevation evaluated at $\eta = 0.66\eta_{max}$ (prior to the crest).

The top subplot of Fig. 10 also includes the linearized wave which is input to the analytical models; the measured wave is clearly steeper, with shallower troughs and higher crests. The linearized wave was obtained by low-pass filtering of the measured wave elevation with a cut-off frequency $\omega_{cut} = \sqrt{\frac{2g}{H_s}}$ [28].

One can also observe such steep waves in the simulation domain in Fig. 9, and these waves cannot be expected to follow the linear dispersion relation. This supports the conclusion that the difference in the location is mainly due to the dispersion error which was described in Section 2. Convergence studies and careful selection of the grid parameters have been used, however, it is impossible to guarantee that one has completely eliminated all numerical uncertainties, especially when working with steep and breaking waves.

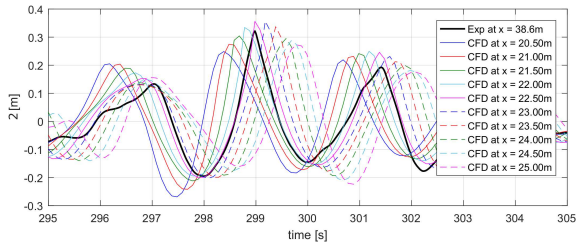

Fig. 8. Comparison of the free surface elevation at several locations against model test time series, CFD reproduction of event A vs. experiment

Table 2. Wave elevation comparisons, Event A.

	Exp.	CFD
Crest height [m]	0.331	0.356
Rise time [s]	0.42	0.39
Steepness [m/s]	0.89	1.16

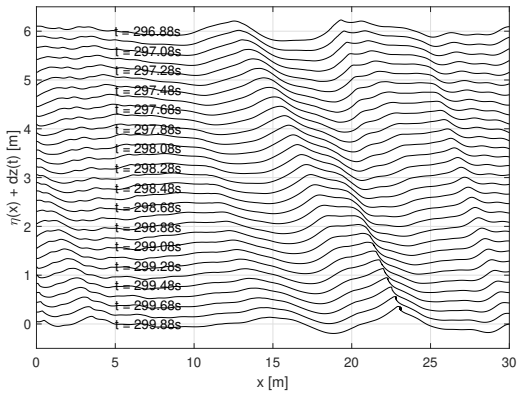

Fig. 9. Visualization of the space-time history of the CFD free surface elevation in event A

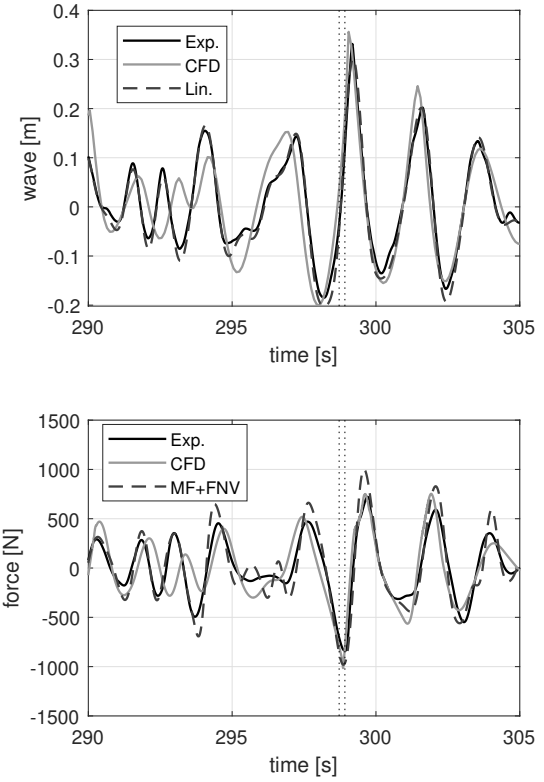

Fig. 10. Wave elevation (measured calibrated wave, CFD calibration reproduction, linearized measured wave) and corresponding force on the cylinder, event A. Thin vertical dotted lines refer to the time instants shown in Fig. 11.

7.1.2 Hydrodynamic force

Based on the wave calibration simulation, the location of the cylinder's center was moved from 20 m to 22.5 m from the wave maker in the CFD simulation for the best match. The hydrodynamic force from the CFD simulation is presented together with the experiment and the analytical models in Fig. 10.

There is generally good agreement between the experimental time series and the CFD results for the hydrodynamic force in Fig. 10, while the analytical models overpredict the peak force significantly. One can observe that the CFD-calibrated wave is slightly steeper and larger than the measured one, which explains the difference in the peak amplitudes between the numerically estimated loads and the measured loads. The shape and phase of the CFD loads agree well with the experimental values, while the analytical model does not display the same shape of the peak.

Fig. 11 presents the CFD fluid visualization during the event. The diffraction effect of the cylinder is visible in the wave pattern of the free surface elevation. The pressure distribution on the cylinder shows the concentration of the wave loads near the free surface, and highlights the fact that the positive force (and response) direction is defined here to be opposite the direction of wave propagation.

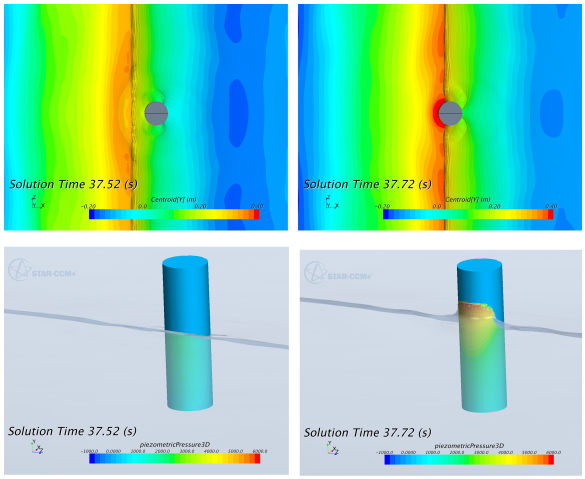

Fig. 11. Fluid visualisation of event A. (Top: free surface elevation; bottom: dynamic pressure distribution). Time stamps differ from the experimental time stamps due to the reduced length of the CFD simulations. The time instants shown here are indicated in Fig. 10 by thin vertical dotted lines.

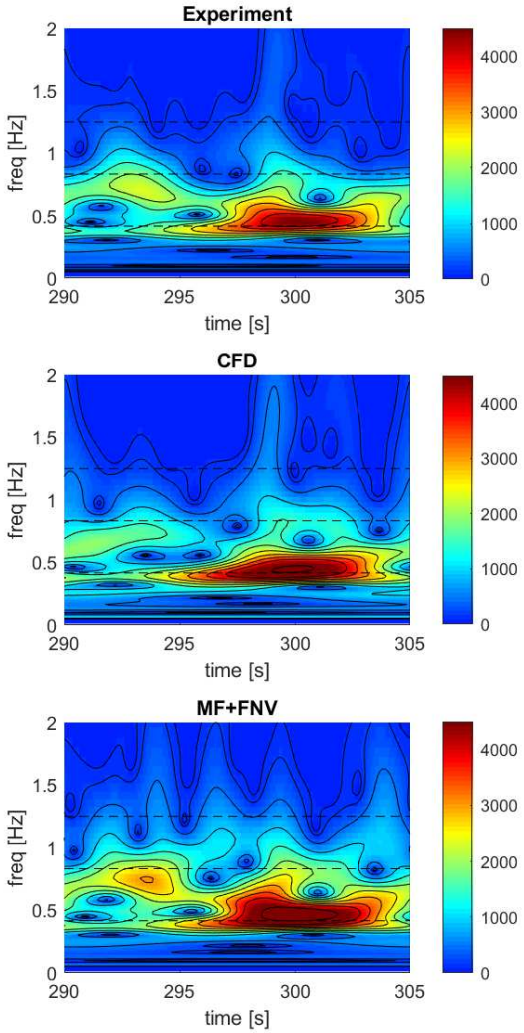

Fig. 12. Wavelet transformation of the horizontal force (N) from experimental measurements (top), CFD (middle) and analytical methods (bottom) for event A. Dashed lines indicate the peak frequency $f_p = 0.42$ Hz, and multiples $2f_p$, $3f_p$.

The frequency content of the hydrodynamic horizontal force from the experiments, CFD, and analytical models is compared in the wavelet transformations shown in Fig. 12. The most significant portion of energy is, as expected, concentrated around the peak frequency (0.42 Hz). Around the severe wave event, one can also observe energy at higher frequencies. Around twice the peak frequency (≈ 0.8 Hz), the analytical model greatly overpredicts the energy, while the CFD calculation slighly underpredicts. At even higher frequencies, the CFD model captures the pattern of energy distribution much more closely than the analytical models.

As previously mentioned, the second order component of the FNV force is expected to be conservative, since second order near-field diffraction effects are not included. The magnitude of the three components of the analytical model can be compared in the time domain in Fig. 13. The axes of Fig. 13 are not equal. As shown, the maximum amplitude of the second order component can be large compared to the first order force, but the largest contributions from the second and third order forces do not necessarily correspond with the largest first order force. Rather, large sum-frequency analytical forces are associated with relatively short waves.

The responses of a SDOF oscillator to the horizontal hydrodynamic forces are exemplified in Fig. 14 for selected values of the natural period and damping. For relatively short natural periods (a stiff spring constant), the dynamic amplification is relatively small, while large amplification can be seen for softer systems, which also show significant transient response after the large wave event. Visually, it is clear that the general characteristics of the response of the SDOF oscillator agree well with those of the response to the measured loads for all of the selected natural periods. The analytical

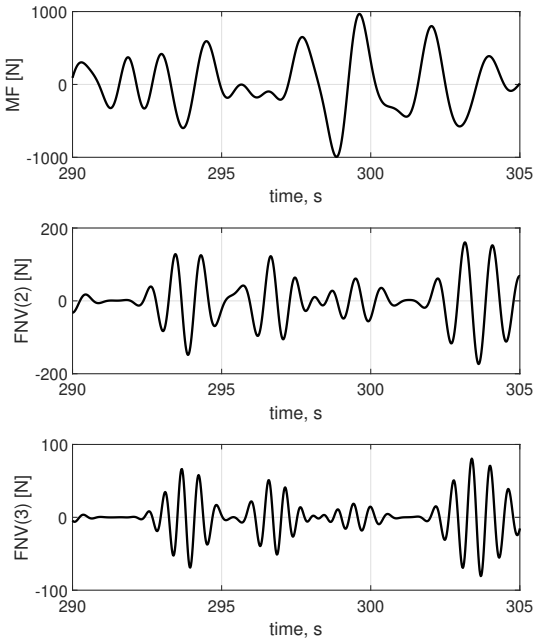

Fig. 13. Components of the hydrodynamic load according to MacCamy-Fuchs (top) and FNV second order (middle) and third order (bottom) for event A.

models do not capture the high-frequency excitation which can excite the stiff SDOF, but give reasonable agreement in the general characteristics of response for $t_n \geq 0.5$ s.

The maximum responses for different oscillators and different models are shown in Fig. 15. The positive responses are seen to be generally slightly larger than the negative responses, although the asymmetry is small. As the damping increases (from top to bottom), the negative maxima decrease, while the positive maxima are nearly unchanged. The comparison between the responses to numerical and experimental load time series suggests that the CFD model gives reasonable predictions of the maxima for the highest and lowest natural periods selected here, but shows some overprediction of the responses for the middle values. The analytical MacCamy-Fuchs + FNV model works best for predicting the maximum responses of stiff systems and is always conservative. These results should however be interpreted together with Fig. 14, which shows that the responses to the CFD loads are qualitatively much more similar to those of the measurements.

Overall, for event A, one can conclude that the CFD is able to reproduce the important physical phenomena. The wave elevation is captured well, and there is good agreement in the magnitude, shape, and frequency content of the loads.

7.2 Event B

7.3 Wave calibration

Wave event B corresponds to the largest high-pass filtered forces from the experimental campaign [10]. The sim-

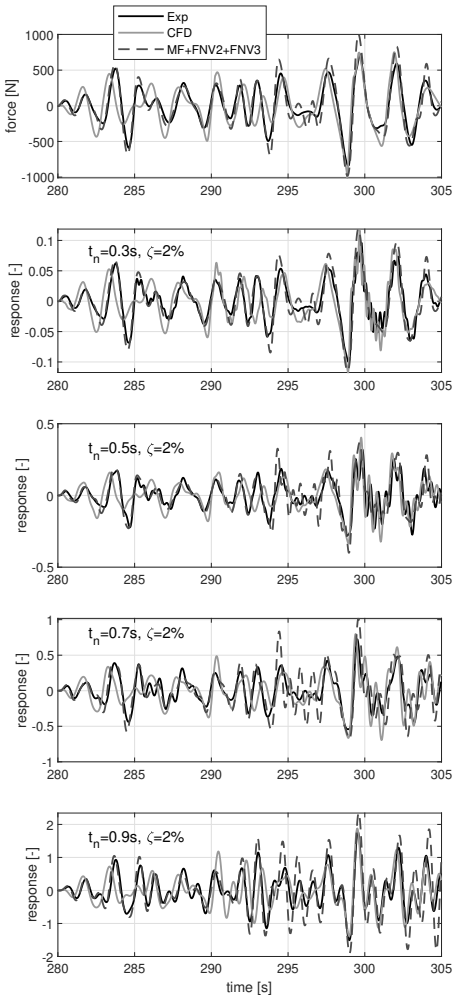

Fig. 14. Time series of the force (top) and response of the SDOF oscillator with various natural periods (t_n) for event A. 2% critical damping is applied in all time series shown here.

ulation of this wave event is challenging because the free surface elevation is recorded after a breaking wave event, as shown in Fig. 16 at x = 18 m and t = 36.4 s. Because breaking wave events are very sensitive to any small changes, it is difficult to repeat such events either experimentally or numerically [15, 29].

The comparison of the numerically estimated time series at different locations against the measured time series is presented in Fig. 17. As shown, the wave event moved in space about 0.75 m upstream from the target location. The agreement between the measured and the numerical wave is worse for event B than for A as far as the steepness and the shape of the wave (see also the top subplot of Fig. 19 and Table 3). In particular, one can observe that the experimental wave is slightly steeper and larger than the numerical one at the front of the wave. On the other hand, after the wave crest, i.e. after t = 422 s, the two waves have almost identical steepness.

The fluid visualization in Fig. 18 shows patterns similar to those of Event A: the diffraction effects can be seen in

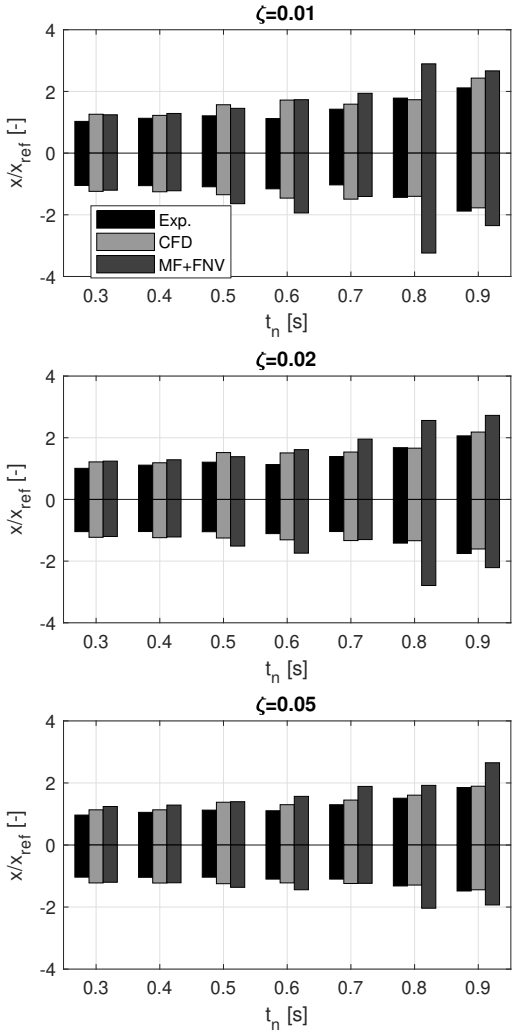

Fig. 15. Comparison of maximum positive and negative responses, event A.

Table 3. Wave elevation comparisons, Event B.

	Exp.	CFD
Crest height [m]	0.307	0.301
Rise time [s]	0.84	0.48
Steepness [m/s]	1.05	0.70

the free surface elevation, while the distribution of pressure shows that the loads are concentrated near the free surface.

7.4 Hydrodynamic force

The hydrodynamic force on the cylinder is shown below the calibrated wave comparison in Fig. 19. The maximum force amplitude from the CFD simulation underpredicts the measured value, which is as expected based on the wave calibration. The shape of the CFD load is similar to that of the experiment, although the phasing is slightly different. The analytical model shows a much higher peak force, but the shape of the peak is not captured.

The wavelet transformation of the force for event B is shown in Fig. 20. As before, the energy content near the

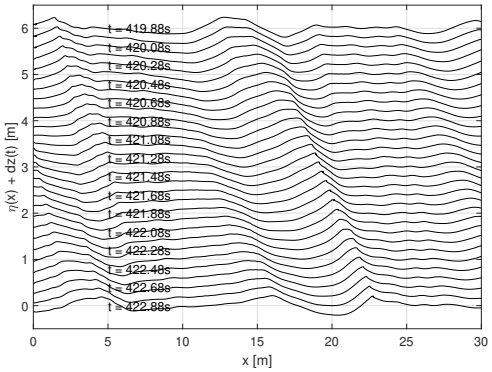

Fig. 16. Visualization of the space-time history of the CFD free surface elevation in event B.

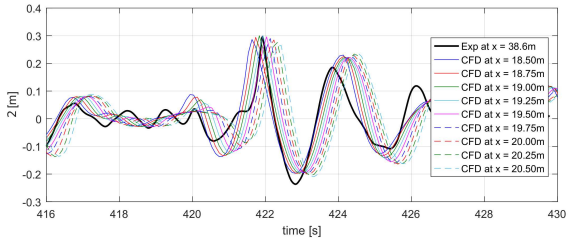

Fig. 17. Comparison of the free surface elevation at several locations against model test time series, CFD reproduction of event B vs. experiment

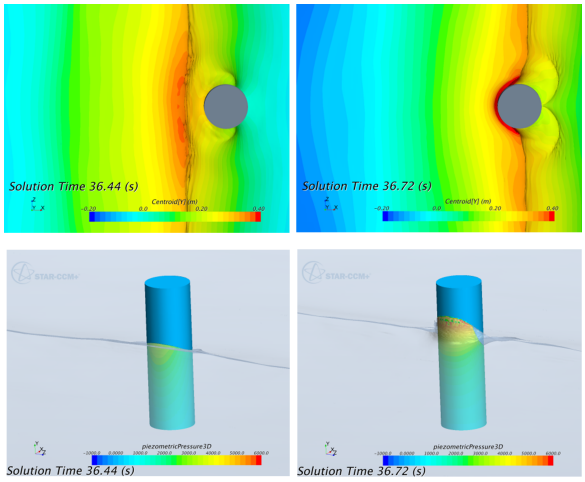

Fig. 18. Fluid visualization of event B. (Top: free surface elevation; bottom: dynamic pressure distribution). Time stamps differ from the experimental time stamps due to the reduced length of the CFD simulations. The time instants shown here are indicated in Fig. 19 by thin vertical dotted lines.

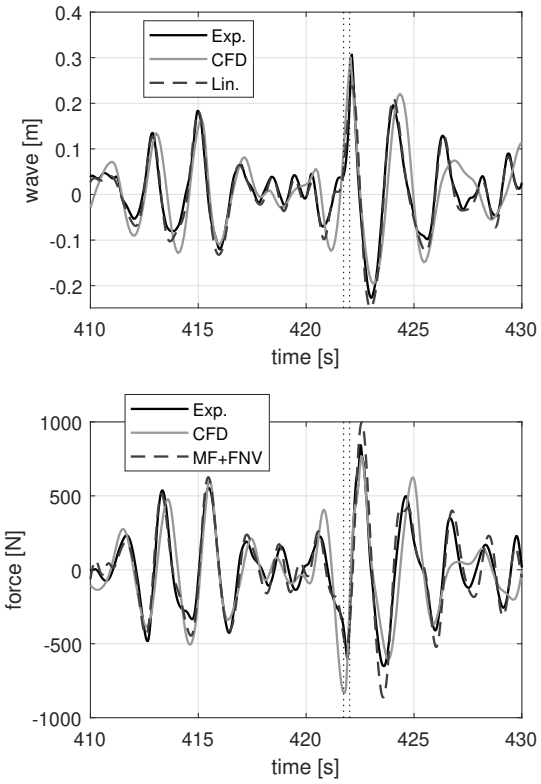

Fig. 19. Wave elevation (measured calibrated wave, CFD calibration reproduction, linearized measured wave) and corresponding force on the cylinder, event B. Thin vertical dotted lines refer to the time instants shown in Fig. 18.

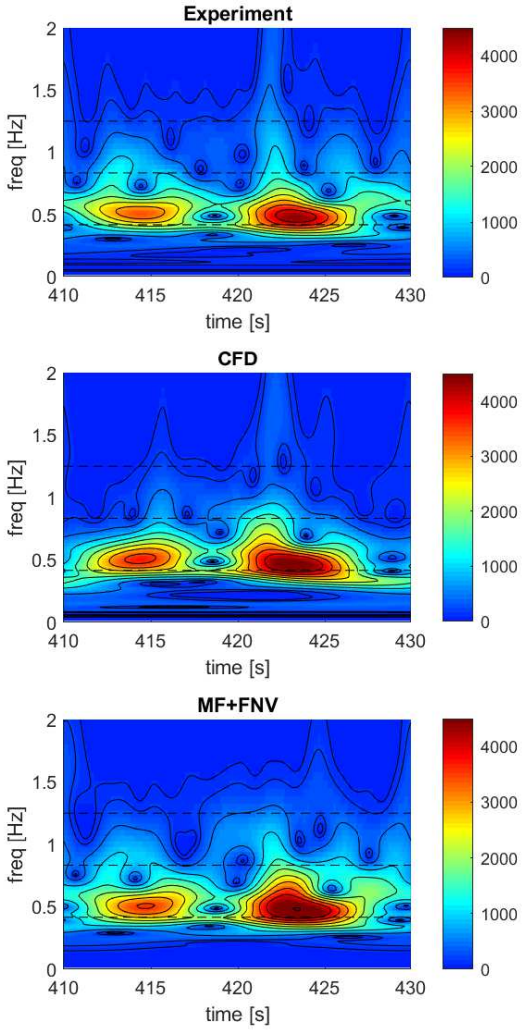

Fig. 20. Wavelet transformation of the horizontal force (N) from experimental measurements (top), CFD (middle) and analytical methods (bottom) for event B. Dashed lines indicate the peak frequency $f_p = 0.42$ Hz, and multiples $2f_p$, $3f_p$.

peak frequency of the waves shows a similar pattern in all three subplots, but there are more significant differences for increasing frequency. The MacCamy-Fuchs + FNV model captures the energy close to the second and third harmonic of the wave periods somewhat better than the CFD model, which underpredicts those high-frequency components in this case. At even higher frequencies, the CFD simulation naturally includes more energy than the analytical model.

The high-frequency content can also be examined through the time series of the SDOF oscillator responses (Fig. 21) and the maximum responses (Fig. 22). Based on Fig. 21, good qualitative agreement in the responses can be seen for the CFD simulations in all cases except the longest period. The analytical model does not capture the transient responses equally well, but the agreement in the magnitude of the response can be seen to be better for the long-period SDOF oscillator. In this case, as shown in Fig. 22, the numerical simulations (CFD and the MacCamy-Fuchs + FNV model) underpredict the responses for $0.4 < t_n < 0.8$ s by up to 30 %. For even higher periods, the second order overprediction from FNV again results in overprediction of the response.

8 Conclusions

It has been shown that it is possible to generate waves numerically using the same approach (and transfer function) as in model tests. In general, good agreement with measurements is shown for both the free surface elevation and the hydrodynamic load.

The comparison of the wave surface elevations shows that the propagation error of the numerical wave, based on the limitations of linear wave theory as well as the numerical error, can be compensated by carefully examining several locations in space and time. The wave event was seen to move 2.5 m downstream in one case, and 0.75 m upstream in the other.

Good agreement is also obtained between the measured and numerically estimated load, which suggests that it is

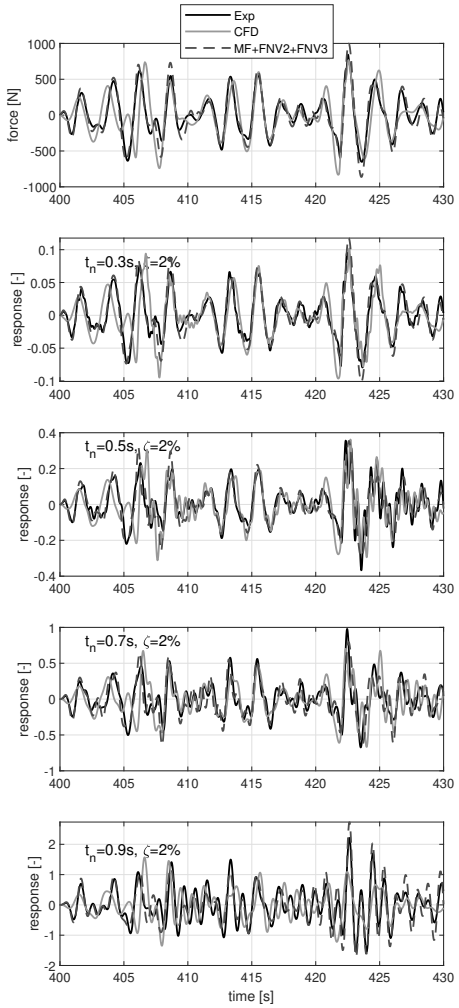

Fig. 21. Time series of the force (top) and response of the SDOF oscillator with various natural periods (t_n) for event B. 2% critical damping is applied in all time series shown here.

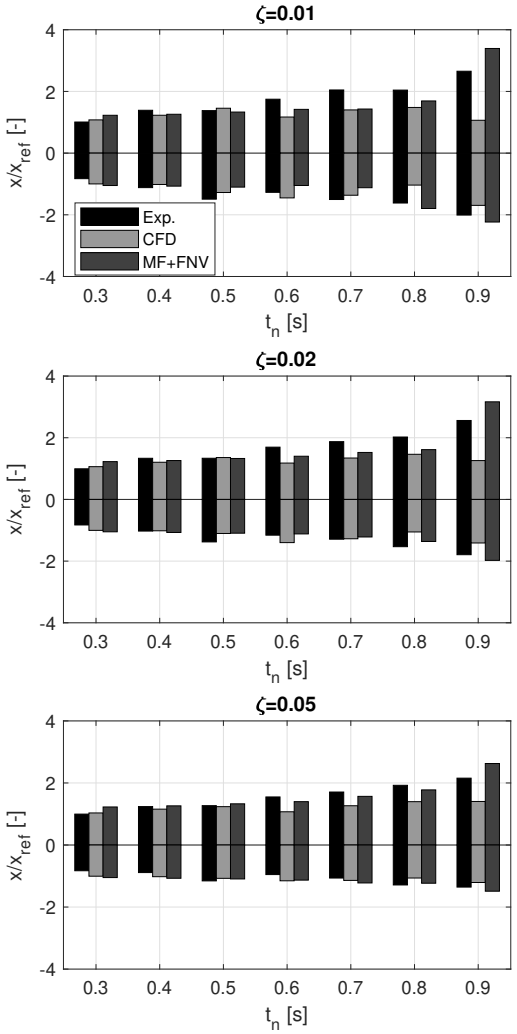

Fig. 22. Comparison of maximum positive and negative responses, event B.

possible to reproduce the correct wave kinematics with this procedure, as long as the wave elevation shows a good match. Based on the wavelet transformation and response of a SDOF, the high-frequency content of the hydrodynamic loads obtained from CFD is similar to that of the experiments. Compared to analytical methods (MacCamy-Fuchs and FNV), the loads from CFD predicted the general behavior of the SDOF much more accurately, although the magnitude of the maximum response was seen to be sensitive to small phase errors. The simple analytical method was able to predict the trends in the maximum responses reasonably well for certain frequencies, and could be more reliable than the CFD method when the match in wave elevation in CFD was poor.

Acknowledgements

This work has been financed by the Norwegian Research Council through a Strategic Research Project at SINTEF Ocean.

References

[1] Faltinsen, O. M., Newman, J. N., and Vinje, T., 1995. "Nonlinear wave loads on a slender vertical cylinder". *Journal of Fluid Mechanics,* **289**, pp. 179–198.

[2] Bachynski, E. E., and Moan, T., 2014. "Ringing loads on tension leg platform wind turbines". *Ocean Engineering,* **84**, pp. 237–248.

[3] Grue, J., Bjørshol, G., and Strand, Ø., 1993. Higher harmonic wave exciting forces on a vertical cylinder. Tech. rep., Preprint Series, Matematisk Institutt Oslo.

[4] Zang, J., Taylor, P. H., Morgan, G., Stringer, R., Orszaghova, J., Grice, J., and Tello, M., 2010. "Steep wave and breaking wave impact on offshore wind turbine foundations - ringing re-visited". In International Workshop on Water Waves and Floating Bodies (IWWWFB25), Harbin, China.

[5] Perić, R., and Abdel-Maksoud, M., 2015. "Assessment

of uncertainty due to wave reflections in experiments via numerical flow simulations". In The Twenty-fifth (2015) International Ocean and Polar Engineering Conference (ISOPE), Kona, Big Island, Hawaii, USA.

[6] Schmittner, C., Kosleck, S., and Hennig, J., 2009. "A phase-amplitude iteration scheme for the optimization of deterministic wave sequences". In Proceedings of the ASME 2009 28th International Conference on Ocean, Offshore and Arctic Engineering, Honolulu, Hawaii, USA, no. OMAE2009-80131.

[7] Bunnik, T., Helder, J., and de Ridder, E. J., 2015. "Deterministic simulation of breaking wave impact and flexible response of a fixed offshore wind turbine.". In Proceedings of the ASME 2015 34th International Conference on Ocean, Offshore and Arctic Engineering, St. John's, NL, Canada, no. OMAE-41989, p. V009T09A049.

[8] Kim, J., O'Sullivan, J., and Read, A., 2012. "Ringing analysis of a vertical cylinder by Euler overlay method". In Proceedings of the ASME 2012 31st International Conference on Ocean, Offshore, and Arctic Engineering (OMAE), Rio de Janeiro, Brazil, no. OMAE2012-84091, pp. 855–866.

[9] Jensen, B., Christensen, E., and Jacobsen, N., 2014. "Simulation of extreme events of oblique wave interaction with porous breakwater structures". In Proceedings of 34th International Conference on Coastal Engineering, Seoul, Korea, P. Lynett, ed., no. 34.

[10] Stansberg, C. T., 1997. "Comparing ringing loads from experiments with cylinders of different diameters - an empirical study". In 8th International Conference on the Behaviour of Off-Shore Structures (BOSS'97), Delft, the Netherlands, Vol. 2, pp. 95–112.

[11] MacCamy, R. C., and Fuchs, R. A., 1954. Wave diffraction on piles: A diffraction theory. Tech. Rep. Technical Memorandum 69, Beach Erosion Board; Corps of Engineers.

[12] Johannessen, T. B., 2012. "Nonlinear superposition methods applied to continuous ocean wave spectra". *Journal of Offshore Mechanics and Arctic Engineering,* **134**, pp. 011302–1–011302–14.

[13] Pákozdi, C., Östman, A., Bachynski, E. E., and Stansberg, C. T., 2016. "CFD reproduction of model test generated extreme irregular wave events and nonlinear loads on a vertical column". In Proceedings of the 35th International Conference on Ocean, Offshore and Arctic Engineering, Busan, Korea, no. OMAE2016-54869, p. V002T08A024.

[14] Pákozdi, C., Kendon, T., and Stansberg, C., 2011. "Breaking wave impact on a platfrom column: an introductory CFD study". In Proceedings of the 30th International Conference on Ocean, Offshore and Arctic Engineering, Rotterdam, the Netherlands, no. OMAE2011-49976, pp. 645–654.

[15] Östman, A., Pákozdi, C., Stansberg, C., Fagertun, J., and Vestbostad, T., 2015. "CFD simulation and validation of breaking wave impact events in irregular sea states". In The Twenty-fifth (2015) International Ocean and Polar Engineering Conference (ISOPE), Kona, Big island, Hawaii, USA.

[16] Pákozdi, C., Perić, M., Lu, H., Baarholm, R., Östman, A., and Stansberg, C. T., 2015. "Estimation of wave in deck load using CFD validated against model test data". In The Twenty-fifth (2015) International Ocean and Polar Engineering Conference (ISOPE), Kona, Big island, Hawaii, USA.

[17] Pákozdi, C., Kendon, T., and Stansberg, C., 2012. "A numerical study of a focused wave packed near the surf zone". In Proceedings of the 31st International Conference on Ocean, Offshore and Arctic Engineering, Rio de Janeiro, Brazil, no. OMAE2012-83796, pp. 619–629.

[18] Clauss, G. F., and Steinhagen, U., 1999. "Numerical simulation of nonlinear transient waves and its validation by laboratory data". In Proceedings of the Ninth (1999) International Offshore and Polar Engineering Conference, Brest, France, pp. 368–375.

[19] Newman, J. N., 1996. *Waves and nonlinear processes in hydrodynamics*. Kluwer, ch. Nonlinear scattering of long waves by a vertical cylinder, pp. 91–102. Oslo, Norway.

[20] Krokstad, J., Stansberg, C., Nestegård, A., and Marthinsen, T., 1998. "A new nonslender ringing load approach verified against experiments". *Transactions of the ASME Journal of Offshore Mechanics and Arctic Engineering,* **120**(1), pp. 20–29.

[21] Marthinsen, T., Stansberg, C. T., and Krokstad, J. R., 1996. "On the ringing excitation of circular cylinders". In the Sixth International Offshore and Polar Engineering Conference, Los Angeles, USA, Vol. 1, pp. 196–204.

[22] Massel, S. R., 2001. "Wavelet analysis for processing of ocean surface wave records". *Ocean Engineering,* **28**, pp. 957–987.

[23] Johannessen, T. B., Haver, S., Bunnik, T., and Buchner, B., 2006. "Extreme wave effects on deep water TLPs: Lessons learned from the Snorre A model tests". In Proceedings on Deep Offshore Technology, Houston, TX, USA.

[24] Niedzwecki, J. M., and Huston, J. R., 1992. "Wave interaction with tension leg platforms". *Ocean Engineering,* **19**(1), pp. 21 – 37.

[25] Kibbee, S. E., Leverette, S. J., Davies, K. B., and Matten, R. B., 1999. "Morpeth SeaStar mini-TLP". In Offshore Technology Conference, Houston, TX, USA, no. OTC 10855.

[26] Chakrabarti, S. K., and Hanna, S. Y., 1990. "Added mass and damping of a TLP column model". In Offshore Technology Conference, Houston, TX, USA, no. OTC 6406, pp. 559–571.

[27] Davies, K. B., Leverette, S. J., and Spillane, M. W., 1994. "Ringing response of TLP and GBS platforms". In Seventh International Conference on the Behaviour of Offshore Structures, Cambridge, MA, USA, Vol. 2, pp. 569–585.

[28] Stansberg, C. T., Gudmestad, O. T., and Haver, S. K.,

2008. “Kinematics under extreme waves”. *Journal of Offshore Mechanics and Arctic Engineering,* **130**(2), p. 021010.

[29] Pákozdi, C., Visscher, J., Stansberg, C., and Fagertun, J., 2015. “Experimental investigation of global wave impact loads in steep random seas”. In The Twenty-fifth (2015) International Ocean and Polar Engineering Conference, Kona, Hawaii, USA.